TRANSIENT VISCOUS FLOW AROUND AN ELLIPTIC CYLINDER

Gary Arthur Roediger

Illinois University

Prepared for:

Office of Naval Research

June 1974

UILU-ENG 74-2216

TRANSIENT VISCOUS FLOW AROUND AN ELLIPTIC CYLINDER

by

Gary Arthur Roediger

This work was supported by the Office of Naval Research under Contract ONR N00014-67-A-0305-0019.

Urbana, Illinois

ib

AD 782 098

Security Classification

DOCUMENT CONTROL DATA - R & D

(Security classification of title, body of abstract and indexing annotation must be entered when the overall report is classified)

1. ORIGINATING ACTIVITY (Corporate author) Coordinated Science Laboratory University of Illinois at Urbana-Champaign Urbana, Illinois 61801	2a. REPORT SECURITY CLASSIFICATION UNCLASSIFIED 2b. GROUP

3. REPORT TITLE

TRANSIENT VISCOUS FLOW AROUND AN ELLIPTIC CYLINDER

4. DESCRIPTIVE NOTES (Type of report and inclusive dates)

5. AUTHOR(S) (First name, middle initial, last name)

Gary Arthur Roediger

6. REPORT DATE June, 1974	7a. TOTAL NO. OF PAGES 47	7b. NO. OF REFS 7
8a. CONTRACT OR GRANT NO. b. PROJECT NO. c. d.	9a. ORIGINATOR'S REPORT NUMBER(S) T-13 9b. OTHER REPORT NO(S) (Any other numbers that may be assigned this report) UILU-ENG 74-2216	

10. DISTRIBUTION STATEMENT

11. SUPPLEMENTARY NOTES	12. SPONSORING MILITARY ACTIVITY Office of Naval Research

13. ABSTRACT

This paper presents a study of the transient flow of a compressible viscous gas around an elliptic cylinder which smoothly accelerates to a fixed velocity. The complete time-dependent Navier-Stokes equations are solved numerically in the body reference frame using a non-orthogonal time-dependent curvilinear coordinate system designed to describe the body exactly and to resolve the important features of the transient flow. The computation is performed in a fixed mesh which maps into a grid in physical space which evolves to accommodate the transient flow.

54

DD FORM 1 NOV 65 1473

Security Classification

14 KEY WORDS	LINK A		LINK B		LINK C	
	ROLE	WT	ROLE	WT	ROLE	WT
Computational fluid dynamics						
Viscous flow						
Navier-Stokes equation						

TRANSIENT VISCOUS FLOW AROUND AN ELLIPTIC CYLINDER

BY

GARY ARTHUR ROEDIGER
B.S., University of Illinois, 1972

THESIS

Submitted in partial fulfillment of the requirements
for the degree of Master of Science in Computer Science
in the Graduate College of the
University of Illinois at Urbana-Champaign, 1974

Urbana, Illinois

ACKNOWLEDGMENT

I wish to thank my thesis advisor, Professor D. Watanabe, for his guidance and valuable discussions in this research and for his many suggestions in preparing the final manuscript. I am indebted to and express special thanks to Professor S. M. Yen for suggesting and supporting this research, for his guidance, encouragement, and many helpful suggestions.

I would also like to recognize Rich Flood who first wrote the Navier-Stokes equations in conservative form for a fixed elliptical cylindrical system and did initial programming in that respect and thanks to Terry Akai for his many helpful comments.

I express deep gratitude to the Coordinated Science Laboratory whose facilities made this research and manuscript possible and to Trudy Williams who typed this thesis.

To my wife, Barbara, I express my thanks for her encouragement and perseverance.

Most of all I wish to recognize my Lord and Savior, Jesus Christ, as my source of all ability and guide to all opportunities.

TABLE OF CONTENTS

Page

1. INTRODUCTION. 1

2. DESCRIPTION OF PROBLEM AND METHOD OF SOLUTION..... 3

2.1. Formulation of the Problem..... 3
2.2. Adaptive Coordinate System..... 4
2.3. Coordinate System..... 7
2.4. Node Distribution..... 10

3. NUMERICAL METHOD AND IMPLEMENTATION..... 14

3.1. Exterior Flow Field..... 15
3.2. Flow at the Body..... 17
3.3. Computer Simulation..... 19

4. NUMERICAL RESULTS..... 22

APPENDIX..... 40

A. Navier-Stokes Equations, Accelerated Reference Frame..... 40
B. Navier-Stokes Equation in Elliptic Coordinates..... 44

LIST OF REFERENCES..... 47

1. INTRODUCTION

Computational fluid dynamics is a new branch of physical science which has developed into a powerful tool with the advent of large scale digital computers. The complex gas dynamic equations can now be solved numerically to simulate gas flows under controlled flow conditions. Computers have indeed become "numerical wind-tunnels." Roache [1] presents a survey of previous work in this field.

This paper presents a study of the transient flow of a compressible viscous gas around an elliptic cylinder which smoothly accelerates to a fixed velocity. The complete time-dependent Navier-Stokes equations are solved numerically in the body reference frame using a non-orthogonal time-dependent curvilinear coordinate system designed to describe the body exactly and to resolve the important features of the transient flow. The computation is performed in a fixed mesh which maps into a grid in physical space which evolves to accommodate the transient flow.

Chapter 2 presents the formulation of the problem and a qualitative description of the transient flow, and outlines the development of a flexible quasi-elliptical time-dependent coordinate system appropriate to the problem. Chapter 3 presents a description of the second order accurate numerical scheme used and a discussion of the computer implementation of the scheme. Finally Chapter 4 presents numerical results for Mach number .169 and local Reynolds number 40 for two cylinders, a nearly circular cylinder of eccentricity .2, and a 2 to 1 elliptic cylinder of eccentricity .866. The results illustrate the development of the boundary layer and

separation and circulation regions and the evolution of the pressure and flow velocity. The flow velocity field is shown in fixed and accelerated frames.

2. DESCRIPTION OF PROBLEM AND METHOD OF SOLUTION

2.1. Formulation of the Problem

Consider an infinite elliptic cylinder with its major and minor axes aligned with the x and y axes centered at the origin and surrounded by a quiescent compressible viscous gas of infinite volume. The cylinder starts from rest, accelerates smoothly until it reaches a given final velocity, and then continues moving at the final velocity.

The flow produced by the cylinder should have the following features. As the cylinder starts from rest, a weak wave is produced which propagates at the speed of sound. As the ellipse accelerates, mass accumulates in front of the body and cavitation occurs in the rear. When the final velocity is reached, the mass accumulated in front of the body produces a compression wave. Similarly, the void in the rear produces an expansion wave. This phenomenon is very similar to the one dimensional piston problem[2]. As these waves propagate, they interact in a complex way, and eventually a steady state is reached near the body. Our objective is to simulate this flow by solving the complete time-dependent Navier-Stokes equations in the body reference frame.

The smooth acceleration of the cylinder permits the simulation of the transient gas flow as well as the steady flow around the body. In previous studies of exterior flows described by the Navier-Stokes equations, the body was either started impulsively, or the steady inviscid flow was used as the initial flow. These studies were aimed at only the steady flow solution because the transient flow produced by these initial

conditions is physically meaningless. An exception is the study of the transient inviscid flow around a circular cylinder by Moretti[3].

2.2. Adaptive Coordinate System

Cartesian coordinates are best suited for rectangular bodies because the grid can be designed so that the body coincides with grid lines. For curved bodies, however, a rational choice of body nodes leads generally to an irregular Cartesian grid, and the body is only approximated by a piecewise linear curve joining the body nodes. The accuracy of this approximation can be increased by increasing the number of body nodes, but the price paid is a large number of unnecessary nodes and further irregularity in the grid. The situation is further complicated by the existence of a boundary layer which requires additional nodes near the body for resolution.

These problems can be resolved through the use of a curvilinear coordinate system in which the body coincides with grid lines. The natural system for this study is the orthogonal elliptical cylindrical coordinate system (u,v) in the accelerated body reference frame. This coordinate system has other advantages besides exact body representation. A grid in (u,v) with uniform u and v spacing maps into a grid in physical space whose nodes cluster near the body. The concentration of points is highest where the curvature is greatest. These two characteristics of the coordinate system combine to place more nodes in physical space where the gradients in the flow variables are greatest. A typical grid corresponding to a uniform (u,v) grid for an ellipse of eccentricity .866

is shown in Figure 1.

This elliptical coordinate system would be ideal for monitoring small perturbations from the steady state solution. However, the use of this coordinate system for the transient flow studied here leads to unresolvable problems. First, as waves move away from the body, they move into the area where the nodes are widely spaced, and hence they cannot be resolved adequately. Second, at the fixed outer boundary, signals arriving from the body cannot be handled properly. The compression and expansion waves exhibit steep gradients which must be resolved by a locally fine grid, and the signals arriving at the outer boundary must be handled carefully to prevent the creation of spurious waves which can destroy the calculation. Adding nodes in the neighborhood of the waves and at the outer boundary would be one solution, but it is impractical because of computer space and time limitations.

A solution is to introduce a time-dependent non-orthogonal quasi-elliptical coordinate system designed so that the nodes of a fixed rectangular grid in this system map into points in physical space which move to accommodate the transient flow. First u is mapped into a new variable ζ by a bilinear transformation so that the interval along any appropriate v hyperbola from the body to the outer boundary is mapped into [0,1]. Then ζ is mapped into the final variable u^* using a hyperbolic transformation. The outer boundary initially is an ellipse concentric with the body and of the same eccentricity but slightly larger. In the fixed frame, the outer boundary expands uniformly at the speed of sound,

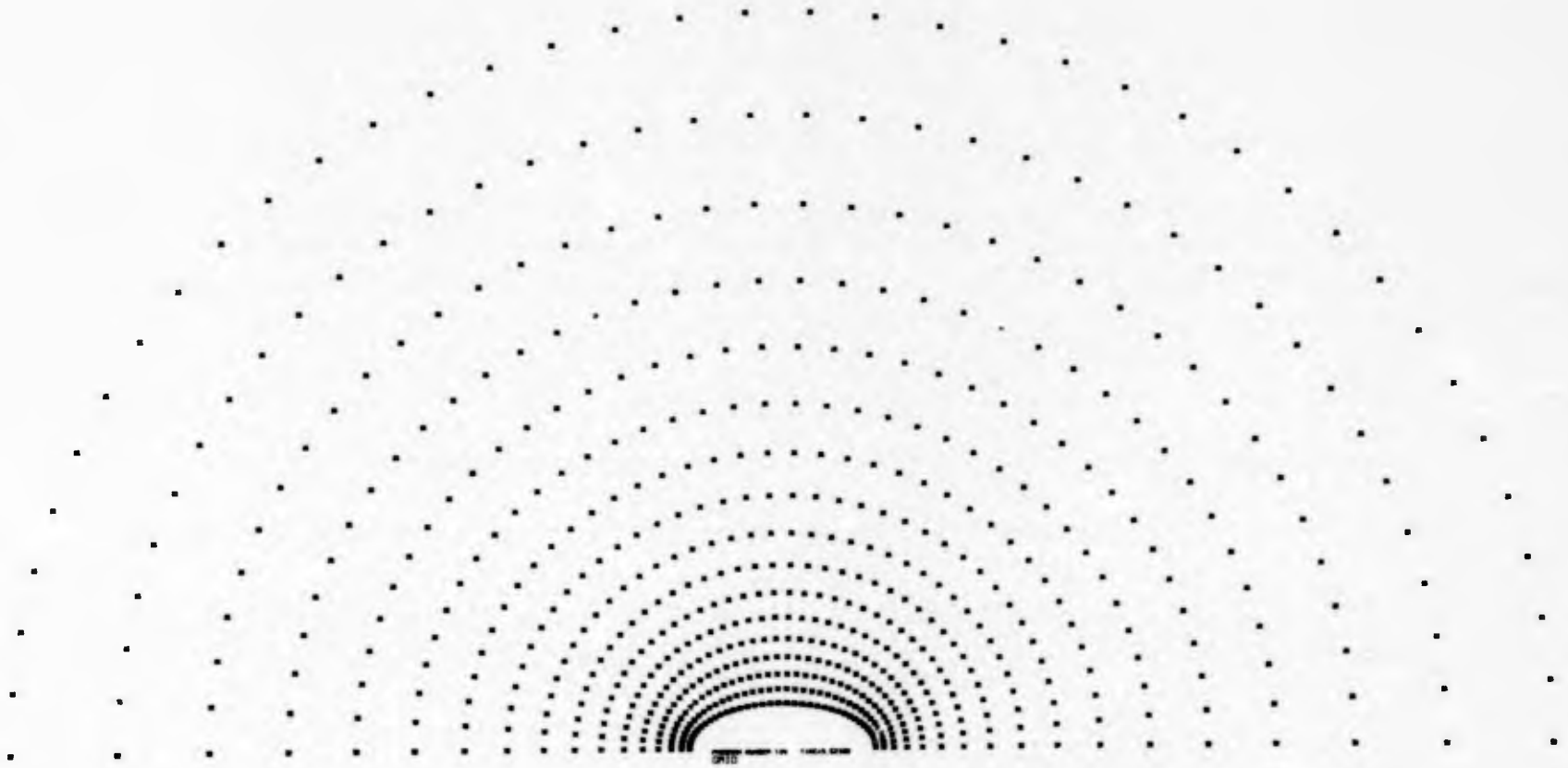

Figure 1. Grid in fixed (u,v) elliptical coordinates.

asymptotically approaching a circle centered at the origin. Hence the signals created by the moving body remain within the computational space. As the calculation proceeds the transformation parameters adjust the mapping so that the fixed grid nodes map into points in physical space clustered about the steep gradients in the flow.

2.3. Coordinate System

The transformation from the fixed frame (x,y) to the accelerating body frame (x*,y*) is given by

$$x^* = x - \int_0^t w_x \, dt \quad ,$$

$$y^* = y - \int_0^t w_y \, dt \quad ,$$

where w_x and w_y are the x and y velocities of the body in the fixed frame. By varying w_x and w_y, the body can move in any direction at any angle attack and at any speed. The conservative form of the Navier-Sokes equations in the accelerating frame with density, momentum, and energy as the primary variables are presented in Appendix A.

The transformation from the coordinates (x*,y*) to the elliptical coordinates (u,v) is given by

$$x^* = c \cosh(u) \cos(v) \quad ,$$

$$y^* = c \sinh(u) \sin(v) \quad .$$

The u and v level curves are confocal ellipses and hyperbolas with foci

(-c,0) and (c,0). An ellipse of eccentricity e is represented by the u level curve for u_o, where

$$u_o = \ln[(1+(1-e^2)^{\frac{1}{2}})/e] \quad .$$

For this ellipse the focal length is c, the semi-major axis is c $\cosh(u_o)$, and the semi-minor axis is c $\sinh(u_o)$. The coordinate u ranges from u_o to ∞ and v ranges from 0 to 2π. Hence this transformation maps the exterior of the ellipse into a semi-infinite strip. The region of interest, however, is a rectangle which lengthens in the u direction with time. The Navier-Stokes equations of Appendix A transformed to elliptical coordinates are presented in Appendix B. In the transformed equations, the terms due to the accelerated reference frame are retained in cartesian form for convenience.

The transformation from u to ζ is given by the bilinear mapping

$$\zeta = (bu+c)/(u+a)$$

where

$$a = [(2u_o-u_1)u_\infty-u_1u_o]/(2u_1-u_o-u_\infty) \quad ,$$

$$b = (u_1+a)/[2(u_1-u_o)] \quad ,$$

$$c = - u_o\, b \quad .$$

This transformation maps the inner boundary u_o, an intermediate point u_1, and the outer boundary u_∞ into 0, 1/2, and 1. Hence it maps the region

of interest into a fixed rectangle.

The final transformation is given by

$$u^* = \frac{1}{2} + \frac{1}{2\alpha} \ln\left[\frac{1+(2\zeta-1)\tanh(\alpha(t)/2)}{1-(2\zeta-1)\tanh(\alpha(t)/2)}\right] ,$$

$$v^* = v ,$$

$$t^* = t .$$

This transformation preserves the fixed rectangular computational space, but is compresses the region in ζ near 1 and 0 and stretches the region near 1/2. The computational space is covered by a fixed uniform rectangular grid which maps into a grid in physical space whose nodes are clustered in the boundary layer, particularly in the regions of greatest body curvature, and near the outer boundary. The parameters u_1 and α are used to control the distribution of the nodes in physical space.

The Navier-Stokes equations are solved on this uniform grid. All factors in the equations other than the derivatives of the flow variables can be easily evaluated analytically. The partial derivatives of the flow variables, however, must be approximated by finite differences. The first partial derivatives of a function f are written in terms of u^* and v^* by applying the chain rules

$$f_u = f_{u^*} u^*_\zeta \zeta_u ,$$

$$f_v = f_{v^*} + f_{u^*} u^*_\zeta \zeta_v ,$$

$$f_t = f_{t^*} + f_{u^*}(u^*_\zeta \zeta_t + u^*_\alpha \alpha_t) .$$

The second partial derivatives are transformed by applying these equations a second time. Then the derivatives of flow variables with respect to u^*, v^*, and t^* are approximated by finite differences on the uniform grid.

2.4. Node Distribution

In the body reference frame, the compression and expansion waves move at different speeds. Hence the outer boundary at u_∞ is a function of v^* and t^*. In the fixed Cartesian frame, the outer boundary is represented by

$$\left(\frac{x}{x_b + c_o t}\right)^2 + \left(\frac{y}{y_b + c_o t}\right)^2 = 1 \quad ,$$

where c_o is the speed of sound in the gas at rest, and x_b and y_b are the semi-major and semi-minor axes of the boundary. Transforming this representation to the accelerated frame moving only in the x direction and scaling distances with respect to $c \cosh(u_o)$ yields the following equation for u_∞,

$$u_\infty(v^*, t^*) = \ln[A + (A^2 - 1)^{\frac{1}{2}}] \quad ,$$

where

$$A = (-C + (C^2 - 4BD)^{\frac{1}{2}})/(2B) \quad ,$$

$$B = (\cos^2(v)E + \sin^2(v)F)/(\cosh^2(u_o)E) \quad ,$$

$$C = (2\, x_d \cos(v))/\cosh(u_o) \quad ,$$

$$D = x_d^2 - (F \sin^2(v))/(E \cosh^2(u_o)) - F \quad ,$$

$$E = (y_b + c_o t)^2 \quad ,$$

$$F = (x_b + c_o t)^2 \quad .$$

Here x_d is the nondimensional distance the ellipse has moved.

The parameters $\alpha(t^*)$ and $u_1(v^*,t^*)$ control the node distribution. The parameter u_1 is chosen so that

$$\frac{\cosh(u_\infty) - \cosh(u_1)}{\cosh(u_\infty) - \cosh(u_o)} = \lambda$$

where λ is a constant between 0 and 1. As λ increases nodes are pulled away from the outer boundary; as λ decreases, nodes are pulled away from the body.

Solving this equation for $u_1(v^*,t^*)$ yields

$$u_1(v^*,t^*) = \ln[A+(A^2 - 1)^{\frac{1}{2}}] \quad ,$$

where

$$A = (1-\lambda)\cosh(u_\infty) + \lambda \cosh(u_o) \quad .$$

Since the outer boundary, u_∞, expands while the total number of nodes remains fixed, the nodes tend to move away from the body. However, the grid in physical space must be fine enough to resolve the boundary layer. Hence a maximum length δ for the distance in physical space between the body and a first u^* node from the body at some value of v^* is specified for each simulation. This length δ, obviously is inversely proportional to the Reynolds number.

The parameter $\alpha(t^*)$ is used to control the spacing of the first row of u^* nodes from the body. The initial value of α is chosen so that the maximum distance, δ, is attained at a given time t_1. For times

smaller than t_1, α is held constant and the spacing increases until it equals δ at time t_1. Thereafter, α is chosen to keep the spacing equal to δ.

By carefully choosing λ and δ, the node distribution can be tailor to the problem needs. For example, in a low Reynolds number flow containing strong waves, λ should be small to concentrate nodes near the waves. In a high Reynolds number flow containing weak waves, λ should be large to concentrate nodes near the body and δ should be small enough to permit adequate resolution of the boundary layer.

A typical node distribution in the (u^*,v^*,t^*) space for some time, $t > 0$, is shown in Figure 2.

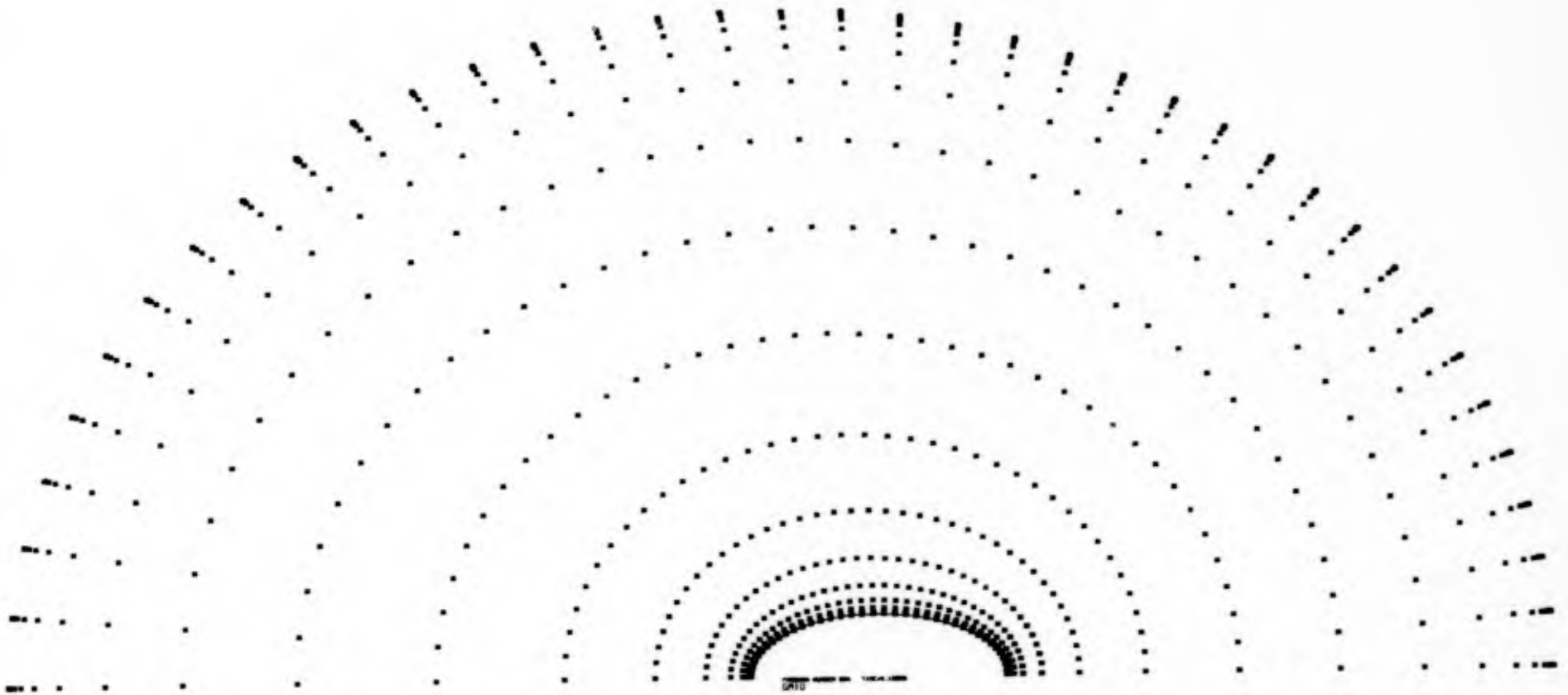

Figure 2. Grid in time dependent coordinate system (u*,v*,t*).

3. NUMERICAL METHOD AND IMPLEMENTATION

The Navier-Stokes equations in the (u^*,v^*,t^*) coordinate system can be written in the form

$$f_{t^*} = G(f_{u^*}, f_{u^*u^*}, f_{v^*}, f_{v^*v^*}, f_{u^*v^*}) \quad .$$

where

$$f = \{\rho, m_u, m_v, E\}^T \quad ,$$

ρ = density ,

m_u = u component of momentum ,

m_v = v component of momentum ,

E = stagnation internal energy .

These equations were solved numerically using MacCormack's predictor-corrector method[4]. This scheme was chosen because it is second order accurate, is easy to implement, and has worked well on viscous flow problems.

Because of computer space and time limitations, the angle of attack is set equal to 0 to exploit the symmetry of the flow about the x-axis. The body velocity w_x is described by the cubic spline with knots 0, $t_f/2$, and t_f satisfying

$$w_x(0) = 0 \quad ,$$

$$w_x(t_f/2) = v_f/2 \quad ,$$

$$w_x(t) = v_f, \quad t \geq t_f \quad .$$

This spline is continuous, has two continuous derivatives, and is anti-symmetric about $(v_f/2, t_f/2)$.

The computational space in (u^*,v^*) is the rectangle $[0,1] \times [0,\pi]$. The grid used is $\{u^*_i, v^*_j\}$ where

$$u^*_i = i\Delta u^*, \quad i = 0, 1, \ldots, M \ ,$$

$$v^*_j = j\Delta v^*, \quad j = 0, 1, \ldots, N \ ,$$

where $\Delta u^* = 1/M$ and $\Delta v^* = \pi/N$. The time is partitioned by the grid $\{t^*_n\}$ where

$$t^*_0 = 0$$

$$t^*_{n+1} = t^*_n + \Delta t^*_n, \quad n = 0, 1, \ldots \ .$$

The value of any function $f(u^*,v^*,t^*)$ at the point (u^*_i, v^*_j) at time t^*_n is denoted by $f^n_{i,j}$.

3.1. Exterior Flow Field

The exterior flow field is defined by $\{u^*_i, v^*_j\}$, i=1, ... , M, and j=0, ... , N. MacCormack's predictor-corrector method first predicts the values of the flow variables at time t^*_{n+1} using

$$\bar{f}^{n+1}_{i,j} = f^n_{i,j} + \Delta t\, G^n_{i,j}, \quad i=1, \ldots, M-1 \text{ and } j=0, \ldots, N \ ,$$

where

$$G^n_{i,j} \equiv G(\Delta_{u^*} f^n_{i,j}, \ \Delta v^* f^n_{i,j}, \ \delta^2_{u^*} f^n_{i,j}, \ \delta^2_{v^*} f^n_{i,j}, \ \Delta_{u^*v^*} f^n_{i,j}) \ ,$$

$$\Delta_{u^*} f_{i,j} = (f_{i+1,j} - f_{i,j})/\Delta u^* \quad ,$$

$$\Delta_{v^*} f_{i,j} = (f_{i,j+1} - f_{i,j})/\Delta v^* \quad ,$$

$$\delta^2_{u^*} f_{i,j} = (f_{i-1,j} - 2f_{i,j} + f_{i+1,j})/\Delta u^{*2} \quad ,$$

$$\delta^2_{v^*} f_{i,j} = (f_{i,j-1} - 2f_{i,j} + f_{i,j+1})/\Delta v^{*2} \quad ,$$

$$\Delta_{u^*v^*} f_{i,j} = (f_{i+1,j+1} - f_{i+1,j} - f_{i,j+1} + f_{i,j})/\Delta u^* \Delta v^* \quad .$$

All the terms in G are evaluated at time t^*_n and the predicted values of the flow variables at the outer nodes are set to the freestream conditions at time t^*_{n+1}.

Then the final values of the flow variables at t^*_{n+1} are obtained using the following correcter equation,

$$f^{n+1}_{i,j} = (f^{n}_{i,j} + \bar{f}^{n+1}_{i,j} + \Delta t \bar{G}^{n+1}_{i,j})/2, \; i=1, \ldots, M-1 \text{ and } j=0, \ldots, N,$$

where

$$\bar{G}^{n+1}_{i,j} \equiv G(\nabla_{u^*} \bar{f}^{n+1}_{i,j}, \nabla_{v^*} \bar{f}^{n+1}_{i,j}, \delta^2_{u^*} \bar{f}^{n+1}_{i,j}, \delta^2_{v^*} \bar{f}^{n+1}_{i,j}, \nabla_{u^*v^*} \bar{f}^{n+1}_{i,j}) \quad ,$$

$$\nabla_{u^*} \bar{f}_{i,j} = (\bar{f}_{i,j} - \bar{f}_{i-1,j})/\Delta u^* \quad ,$$

$$\nabla_{v^*} \bar{f}_{i,j} = (\bar{f}_{i,j} - \bar{f}_{i,j-1})/\Delta v^* \quad ,$$

$$\delta^2_{u^*} \bar{f}_{i,j} = (\bar{f}_{i+1,j} - 2\bar{f}_{i,j} + \bar{f}_{i-1,j})/\Delta u^{*2} \quad ,$$

$$\delta^2_{v^*}\bar{f}_{i,j} = (\bar{f}_{i,j+1} - 2\bar{f}_{i,j} + \bar{f}_{i,j-1})/\Delta v^{*2} \quad ,$$

$$\nabla_{u^*v^*}\bar{f}_{i,j} = (\bar{f}_{i,j} - \bar{f}_{i,j-1} - \bar{f}_{i-1,j} + \bar{f}_{i-1,j-1})/\Delta u^*\Delta v^* \quad .$$

All the terms in $\bar{G}$ are calculated at time t^*_{n+1} and the final values of the flow variables at the outer nodes are set to freestream conditions at time t^*_{n+1}.

Both the predictor and the corrector require the flow variables at $v^*_{-1} = -\Delta v^*$ and $v^*_{N+1} = \pi + \Delta v^*$. These values are obtained by symmetry from the values at v^*_1 and v^*_{N-1} as follows

$$\rho_{i,j} = \rho_{i,j+2}$$

$$(m_u)_{i,j} = (m_u)_{i,j+2}$$

$$(m_v)_{i,j} = -(m_v)_{i,j+2}$$

$$E_{i,j} = E_{i,j+2}$$

for $j = -1$ and $N-1$.

3.2. Flow at the Body

A separate calculation is required to compute the flow variables at the body. The two major conditions imposed on the flow at the body are (1) no-slip at the surface in the accelerated frame, and (2) the wall is adiabatic.

The no-slip or zero particle velocity condition is implemented by setting m_u and m_v to zero at the wall. For an adiabatic wall, the internal energy of the gas, e, at the surface has zero gradient normal to the surface.

$$(e_u)_{body} = 0$$

Now the energy of a perfect gas is

$$E = \rho e + \rho \, \underline{V}\cdot\underline{V}/2 \quad .$$

Since the velocity vector, $\underline{V}$, at the wall is zero, it follows that

$$(E_u)_{body} = (\rho_u e)_{body} = (\rho_u E/\rho)_{body}$$

To be consistent with MacCormack's second order scheme, all derivatives must be approximated by a second order accurate difference formula at the wall. Hence the following equation is used

$$(f_u)_{o,j} = (1/2\Delta u^*)(-3f_{o,j} + 4f_{1,j} - f_{2,j})(u^*\zeta_u)_{o,j} \quad .$$

Substituting this expression for E_u and ρ_u in the equation already given and solving for $E_{o,j}$ yields

$$E_{o,j} = \rho_{o,j}(4E_{1,j} - E_{2,j})/(4\rho_{1,j} - \rho_{2,j}) \quad .$$

In the predictor $\bar{\rho}_{o,j}$ can be calculated using the continuity equation and the predicted energy, $\bar{E}_{o,j}$, is obtained from the equation for $E_{o,j}$ above using predicted values at time t^*_{n+1} on the right hand side.

The boundary calculations in the corrector present a problem since nodes (u^*_{-1}, v^*_j) are needed but do not exist. The required derivatives in the continuity equation must be approximated by a second order accurate difference formula consistent with MacCormack's corrector equation. The following approximation can be used.

$$(\bar{f}_u)_{o,j} = (1/\Delta u^*)(-2\bar{f}_{o,j} + 3\bar{f}_{1,j} - \bar{f}_{2,j})(u^*_\zeta \zeta_u)_{o,j}$$

Using this result in the continuity equation yields the values of $\rho^{n+1}_{o,j}$. The energy, $E^{n+1}_{o,j}$, is then obtained from the equation for $E_{o,j}$ above using corrected values at time t^*_{n+1} on the right hand side.

A second method recommended by Roache[5] for computing the density at the boundary was also used. This method, which employs a staggered mesh, provided results very close to the results of the first method. The method required a large amount of geometric computation because of the time dependent grid and moreover required the solution of a tridiagonal system of linear equations for the density values. Since this method for all its added complexity did not produce significantly different results, it was discarded in favor of the first scheme.

3.3. Computer Simulation

The complexity of the coordinate system, Navier-Stokes equations, and numerical scheme, the small time steps required for stability, and the relatively large number of nodes required for adequate resolution, all combine to require a very large amount of computer time for each

simulation. Another important factor is the amount of internal storage available. Since many time dependent variables in the predictor are identical to those of the previous corrector, these variables can be computed at each node once and used both in the corrector at t_n^* and the predictor at t_{n+1}^* if storage is available. Unfortunately, storage was at a premium on the machines used, and many quantities had to be recomputed. This added to the already large computing times for each simulation.

Initially the outer boundary is a finite distance from the body. Hence calculations are performed only at the nodes within the envelope of the wave created by the initial motion of the cylinder. At the remaining nodes, the flow variables are assigned their freestream values. This procedure saves a large amount of computer time during early times, and works better than the alternative procedure of adding nodes using interpolation.

The numerical scheme was implemented in a Fortran program. Two versions of the program were written: one for the PDP-10 timesharing system, and one for the IBM 360/75 batch system. The basic programs were identical, but the PDP-10 program contains interactive facilities which allow the user to review results dynamically, set checkpoints, and adjust the time step for stability. Both versions automatically adjust the time step to maintain stability. If instability occurs the time step is decreased and the program restarts using the data at the previous stable checkpoint. Checkpoints for program restarts are created by writing the current values of all time dependent variables into a disk file. This procedure minimizes the effect of a machine failure or numerical instability.

The parameters required for a simulation are the reference Reynolds number, eccentricity, grid parameters M and N, node distribution parameters λ, δ, x_b, and t_1, acceleration parameters t_f and V_f, and the initial time step Δt^*. When a run is restarted using a checkpoint of a previous run, Δt^* may be reset. The results are printed on a line printer and plotted, if desired, on a CALCOMP plotter or a Tektronix 4010-1 display.

4. NUMERICAL RESULTS

Calculations were performed for two cylinders, a nearly circular cylinder of eccentricity .2 and a 2 to 1 cylinder of eccentricity .866. In both calculations Δu^* is 1/31, Δv^* is $\pi/37$, λ is .68, δ at $v^* = \pi$ is .008, the Prandel number is .75, γ is 1.4, the reference Reynolds number is 100, the final Mach number is .169 attained at time .5, and the local Reynolds number,

$$Re_\ell = 2c \cosh(u_o)\rho_o w_x(t)/\mu \quad ,$$

is 40 at Mach number of .169.

In both calculations the initial time step is .0001. As the minimum spacing between nodes increases to δ, the time step increases to .001 for the first cylinder and .00095 for the second. Because of the small time steps used, each calculation required a large number of steps and consequently a large amount of time. The first required 15.5 hours on the IBM 360/75 to reach time 11.4 in 13,362 steps, while the second required 18 hours to reach time 13.46 in 15,380 steps!

As the body accelerates, mass accumulates in front of the body and cavitation occurs behind the body. This phenomenon is evident in the 3-dimensional pressure plots in (u^*,v^*) shown in Figures 4 and 5, where the pressure is high in the front and low behind. These two figures also illustrate the effects of viscosity since they are from runs differing only in the reference Reynolds number. The viscosity in Figure 5 is 10 times that in Figure 4. Consequently the smearing of the compression

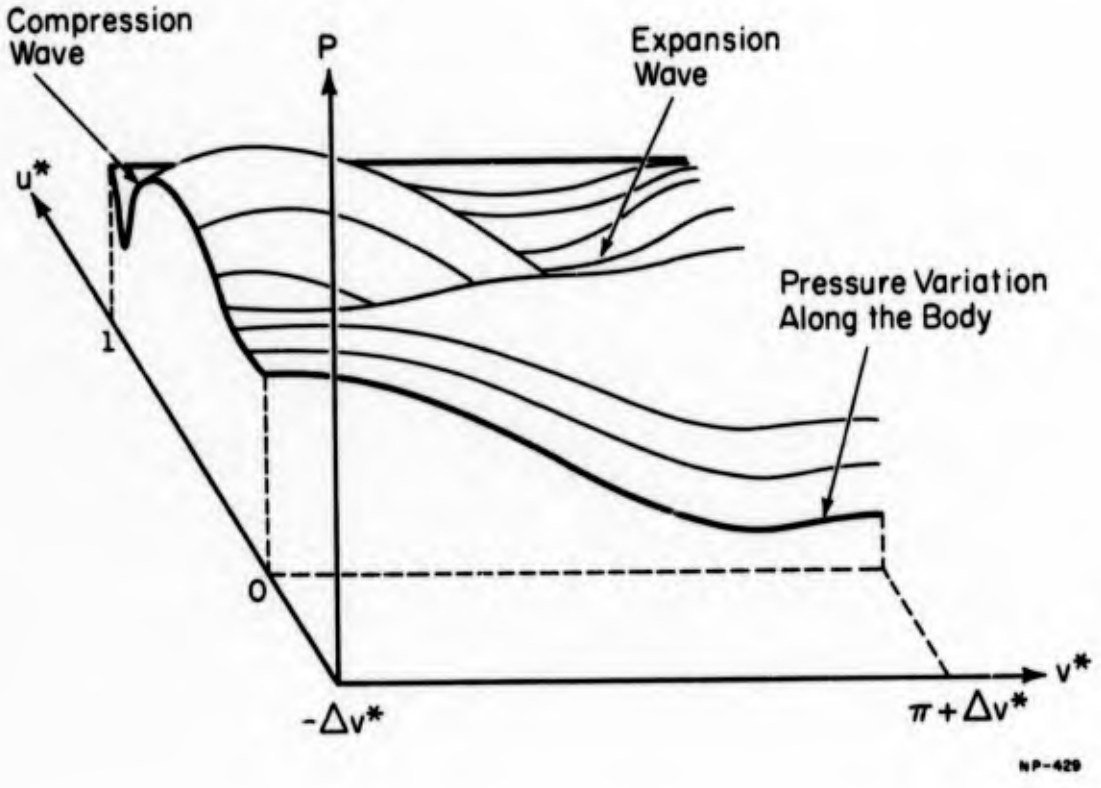

Figure 3. Description of 3-dimension pressure field plots in (u*,v*) space.

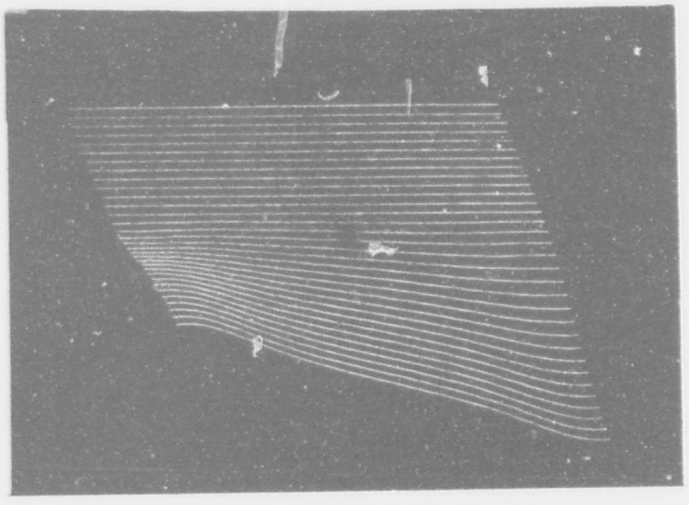

Figure 4. 3-Dimensional pressure plot, eccentricity is .866, Re is 1000, Mach number is .034, and at time .14.

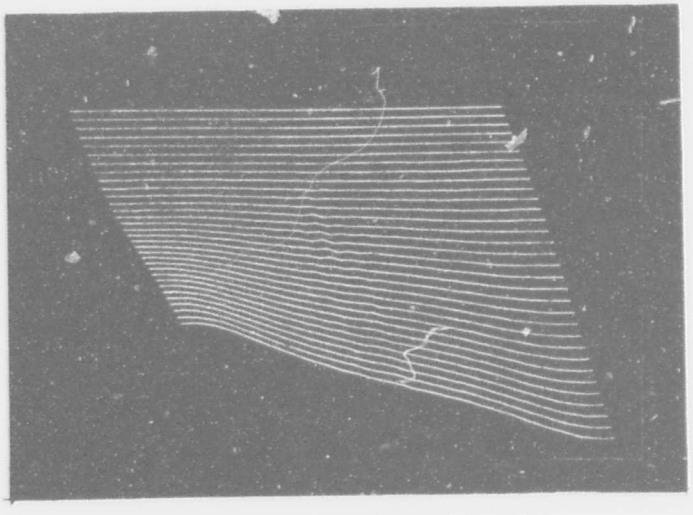

Figure 5. 3-Dimensional pressure plot, eccentricity is .866, Re is 100, Mach number is .104, and at time .29.

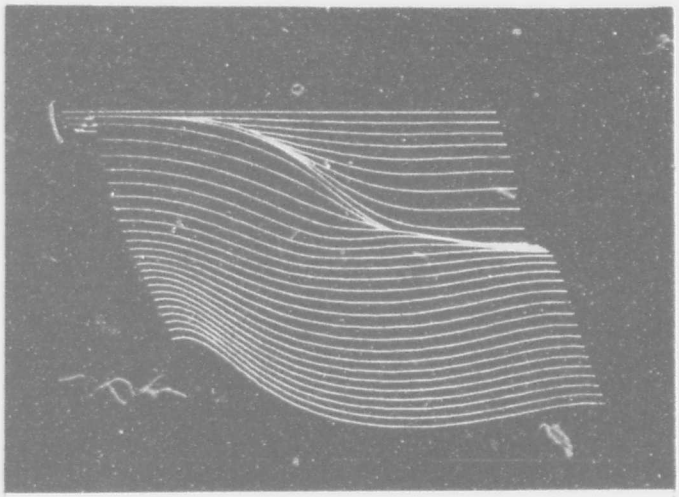

Figure 6. 3-Dimensional pressure plot, eccentricity is .866, Re is 100, Mach number is .169, and at time 2.95.

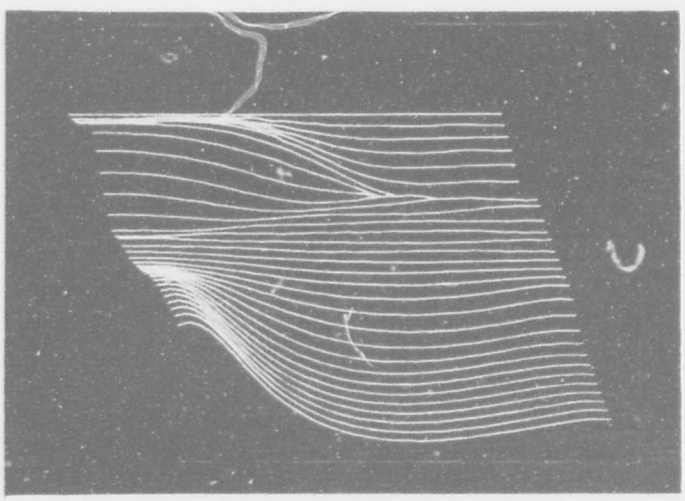

Figure 7. 3-Dimensional pressure plot, eccentricity is .866, Re is 100, Mach number is .169, and at time 10.25.

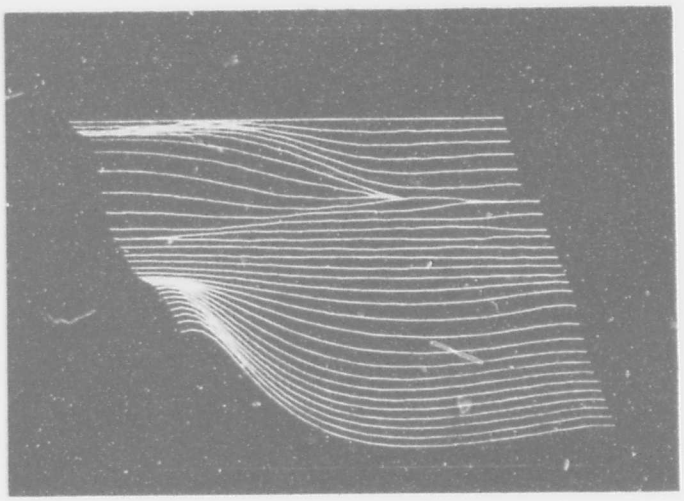

Figure 8. 3-Dimensional pressure plot, eccentricity is .866, Re is 100, Mach number is .169, and at time 13.46.

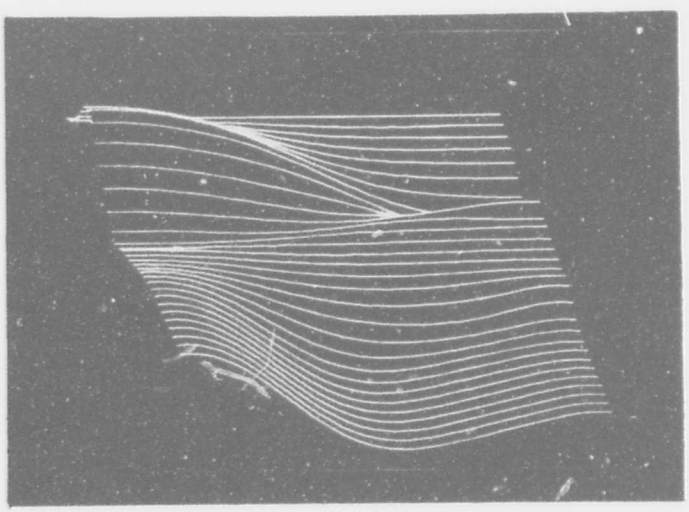

Figure 9. 3-Dimensional pressure plot, eccentricity is .2, Re is 100, Mach number is .169, and at time 10.60.

and expansion waves is greater in Figure 5.

When the final velocity is attained, compression and expansion waves move out from the front and rear of the body at the speed of sound, $\sqrt{\gamma}$. As these waves interact, they create complex waves within the gas. These waves can be seen in Figures 6 and 7. Eventually a steady state is reached near the body. Figures 8 and 9 show the steady state pressure distribution near the body as well as the compression and expansion waves far from the body for both cylinders.

The pressure coefficient is defined as

$$C_p = 2(p-1)/w_x^2 \quad ,$$

where p is the dimensionless pressure and w_x is the dimensionless velocity of the body. The evolution of C_p at the surface of the bodies is shown in Figures 10 through 13. Initially the pressure is high in front and low behind, but as the compression and expansion waves travel around the body and interact, the pressure decreases in front and increases behind and the pressure coefficient reaches the steady state shown in Figure 11 at time 10.60 for the near circle and in Figure 13 at time 13.46 for the 2 to 1 ellipse.

The density variation throughout the flow field is 7% for the near circle and 5% for the 2 to 1 ellipse. The temperature variation at the body is 2% for the near circle and 1% for the 2 to 1 ellipse. The variations for the near circle are larger than those for the 2 to 1 ellipse because the blunter near circle produces stronger compression

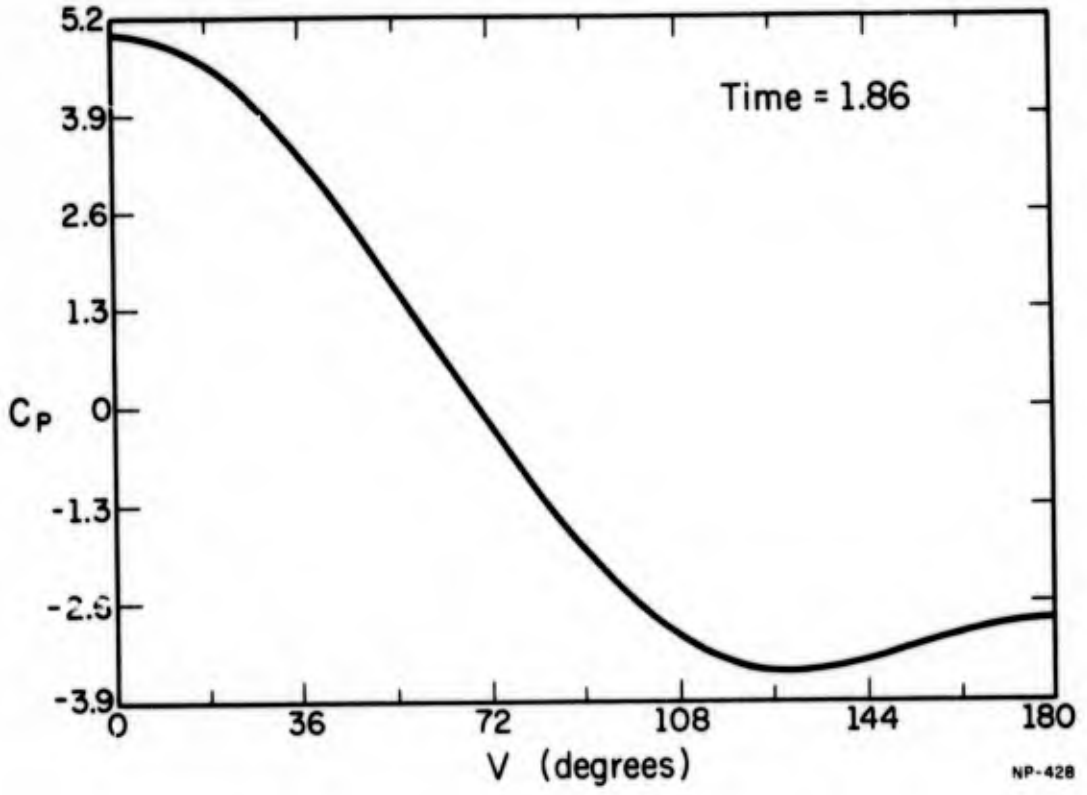

Figure 10. Pressure coefficient around body of eccentricity .2.

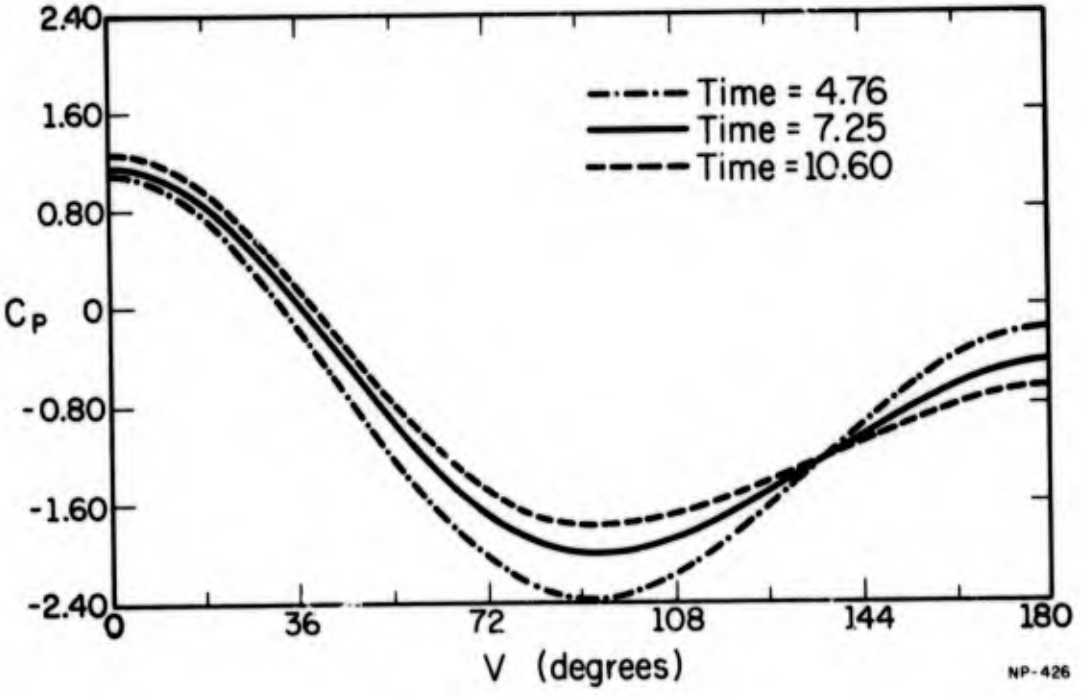

Figure 11. Pressure coefficients around body of eccentricity .2 for various times. Time 10.60 is steady state curve.

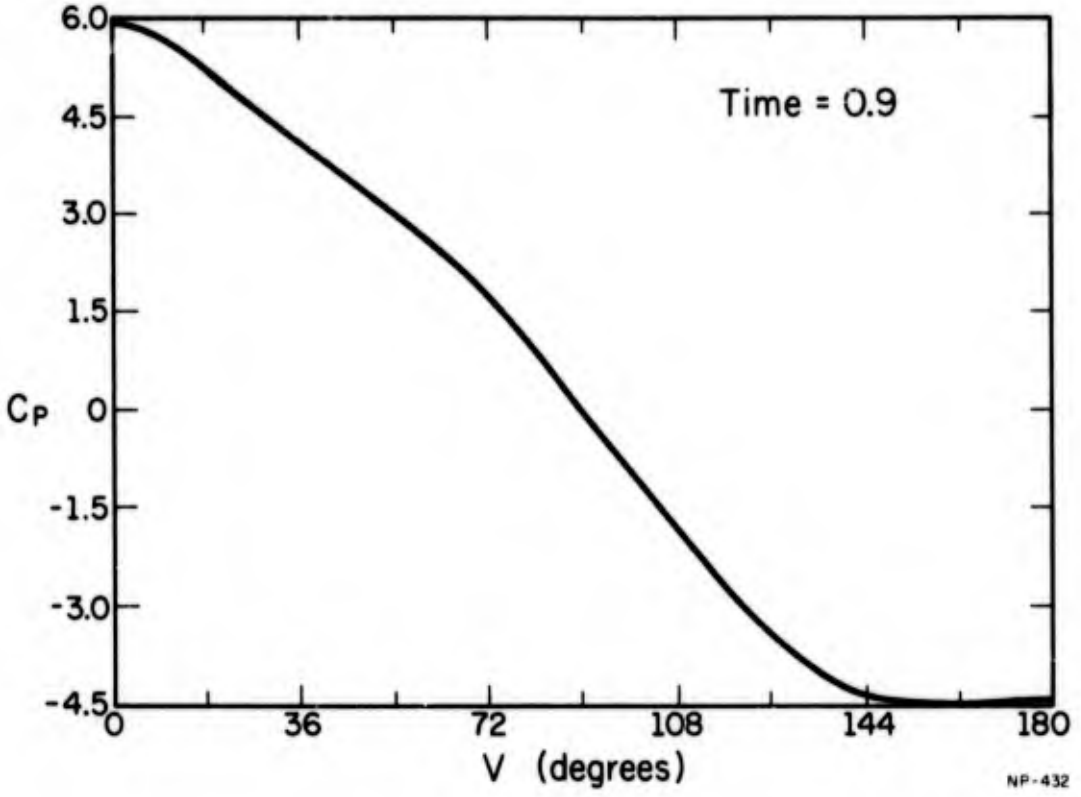

Figure 12. Pressure coefficient around body of eccentricity .866.

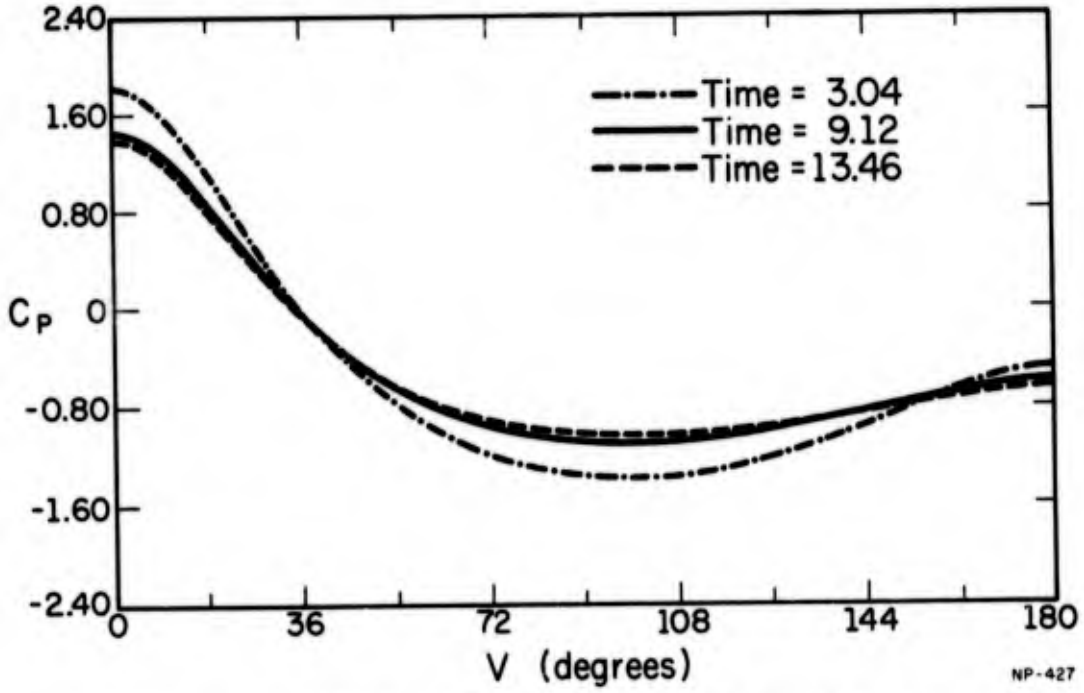

Figure 13. Pressure coefficients around body of eccentricity .866 for various times. Given 13.46 is steady state curve.

and expansion waves. This difference in relative strengths of the waves is evident in the 3-dimensional pressure plots in Figures 8 and 9.

Figures 14 through 22 show the velocity field development in the body reference frame. They illustrate how the boundary layer evolves and how separation and circulation eventually develop. Figures 18 and 22 show that separation occurs further downstream for a slender body than for a blunt body. Let s be the arc length along the body from the front stagnation point and let ℓ be half the body perimeter. Figures 18 and 22 show separation occurring at $\frac{s}{\ell} = .63$ for the near circle and at $\frac{s}{\ell} = .84$ for the 2 to 1 ellipse.

Figures 23 through 29 show the velocity field development in the fixed frame. They illustrate how the accelerating body affects the gas particles. The particles at the surface move in the same direction and at the same speed as the body. The particles in front of the body are pushed out and around the cylinder, while those behind are pulled in toward the body to fill the void. A circulation region develops near $v^* = \pi/2$ during acceleration, and then moves slowly downstream. Figures 23 to 29 illustrate the development of these regions.

These results represent nearly incompressible isothermal flow. In principle this method can also be applied to high subsonic Mach number flows where compressible and thermal effects are more significant. However, finer meshes would be required to resolve the steeper gradients of such flows, and smaller time steps would be required for stability. This might raise the computer storage and processor time to prohibitively high levels on many machines.

Figure 14. Initial boundary layer growth at time .29.

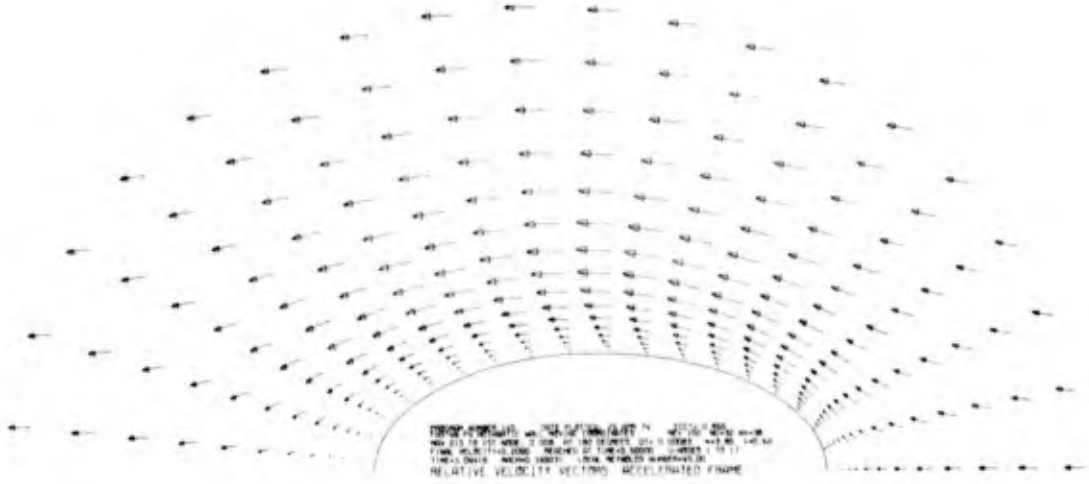

Figure 15. Velocity field development at time 3.04.

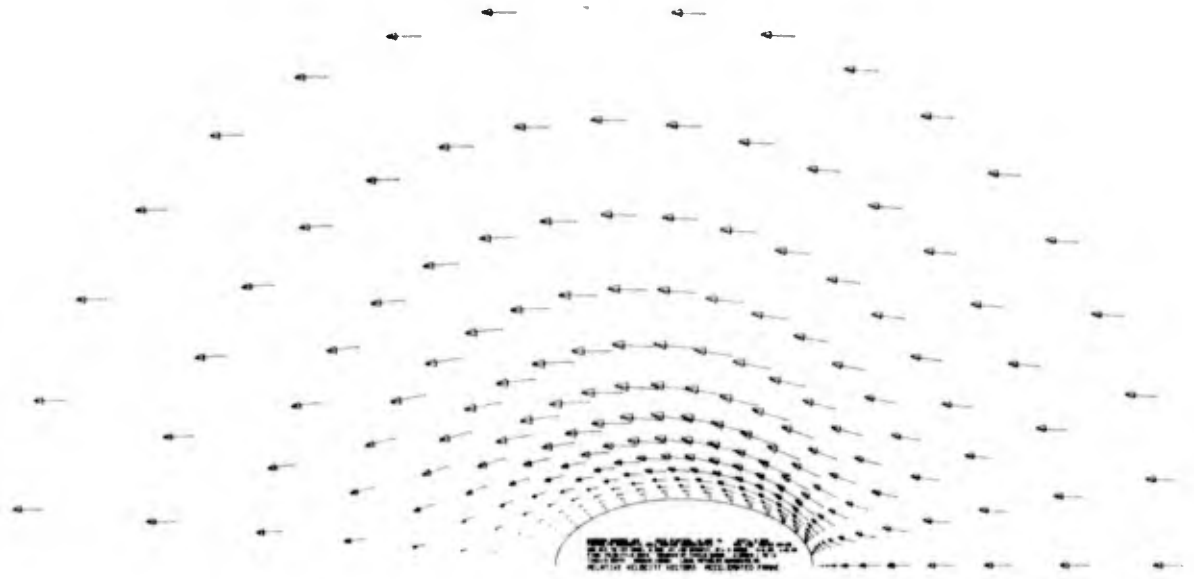

Figure 16. Velocity field development at time 10.25.

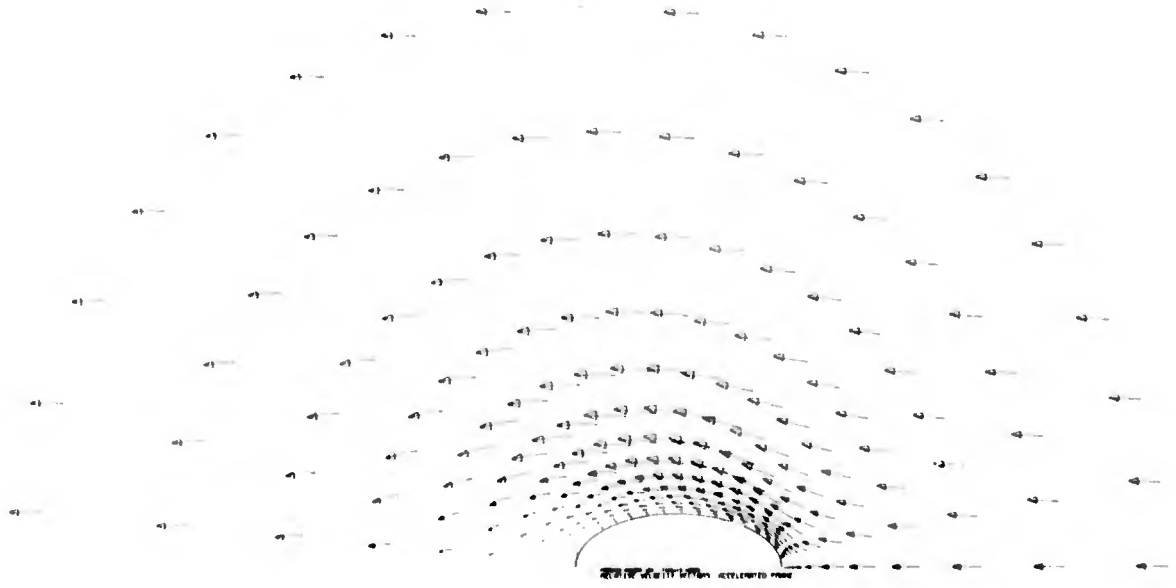

Figure 17. Circulation and separation at time 13.46.

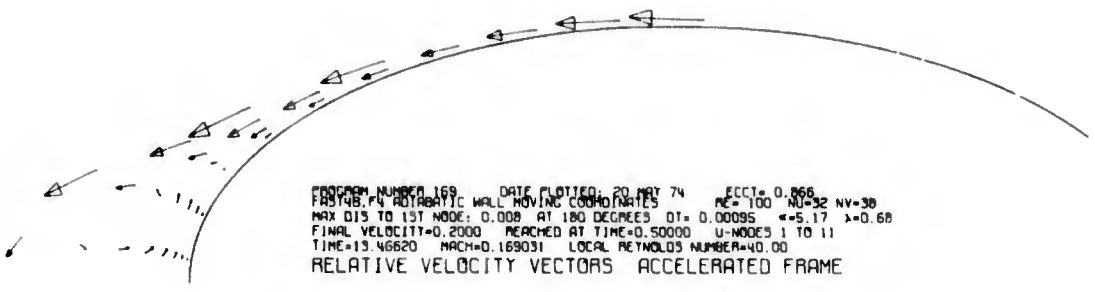

Figure 18. Enlarged view of circulation region at time 13.46.

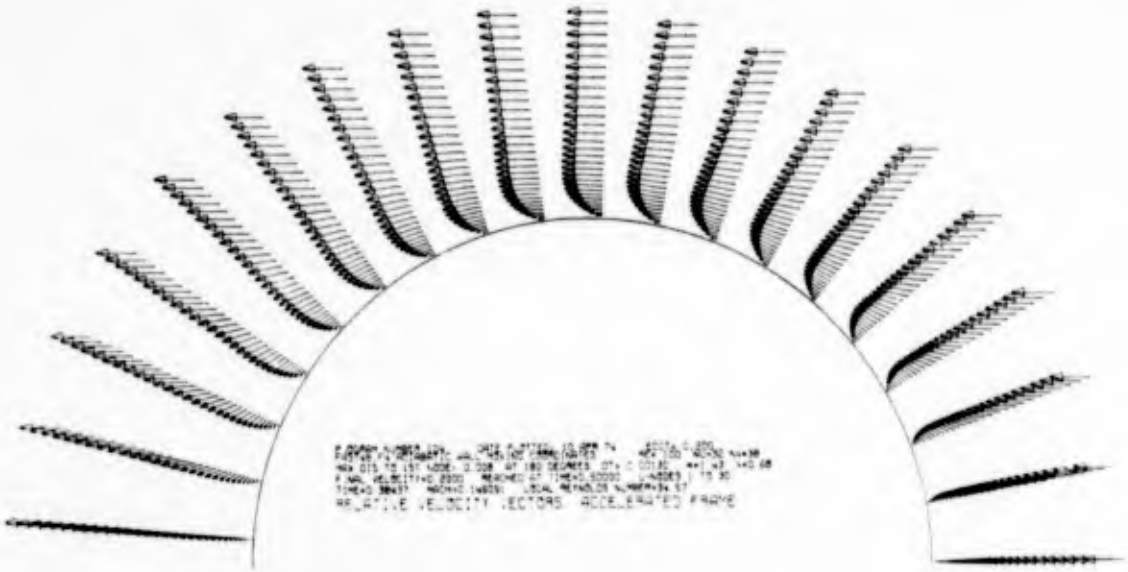

Figure 19. Initial boundary layer growth at time .38.

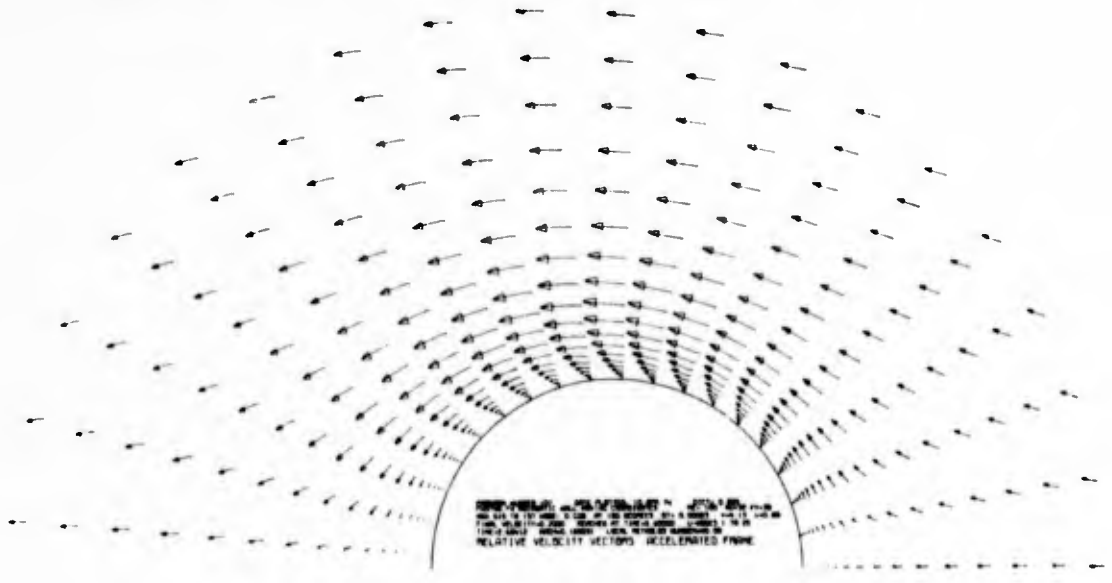

Figure 20. Velocity field development at time 2.69.

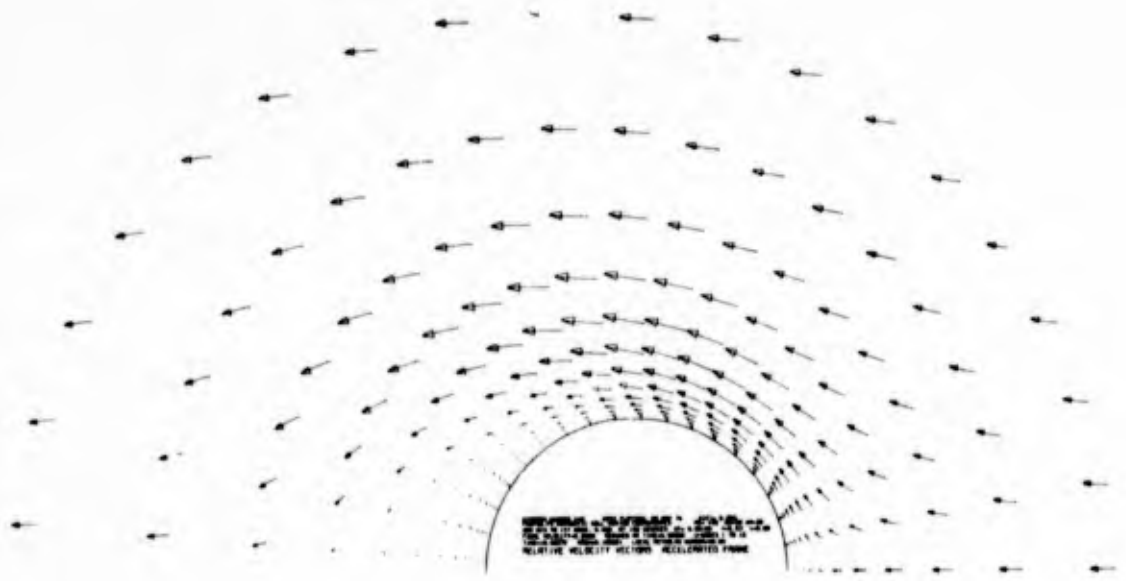

Figure 21. Circulation and separation at time 10.60.

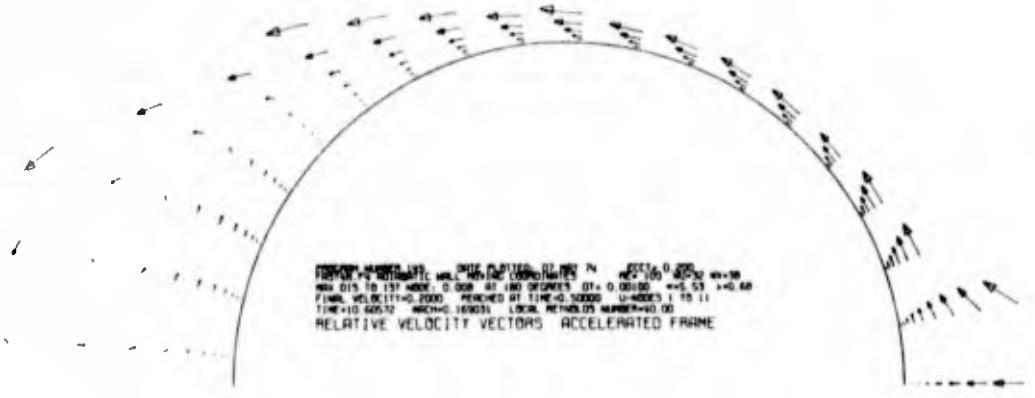

Figure 22. Enlarged view of circulation region at time 10.60.

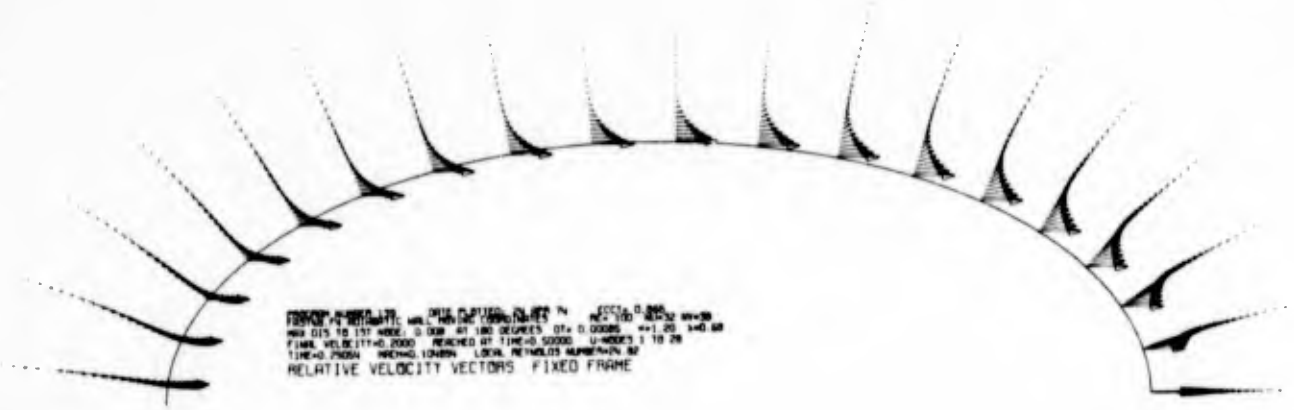

Figure 23. Initial gas particle movement at time .29.

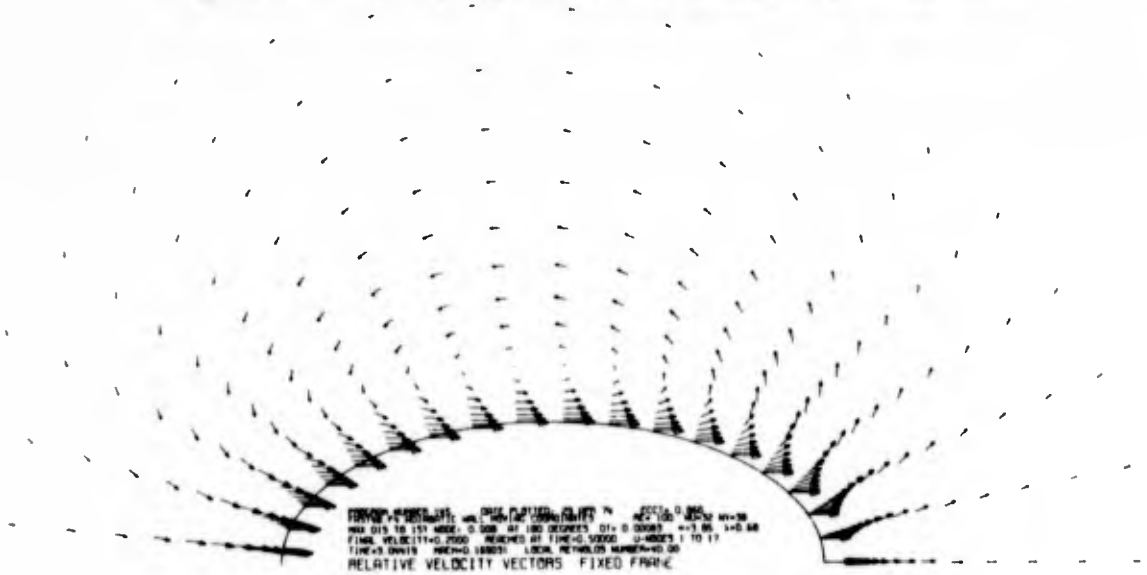

Figure 24. Gas particle movement at time 3.04.

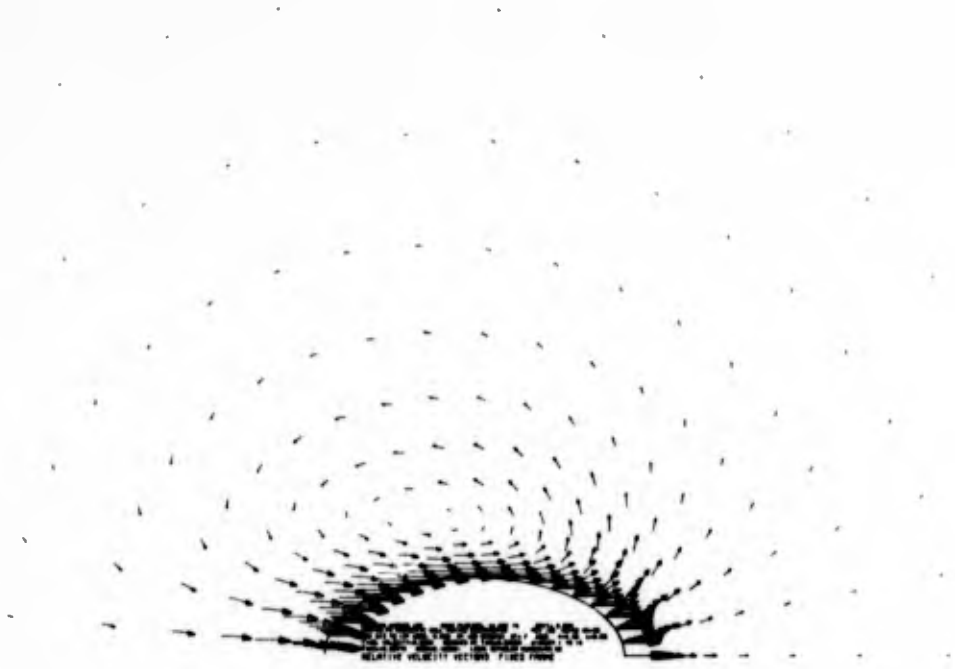

Figure 25. Gas particle movement at time 10.25.

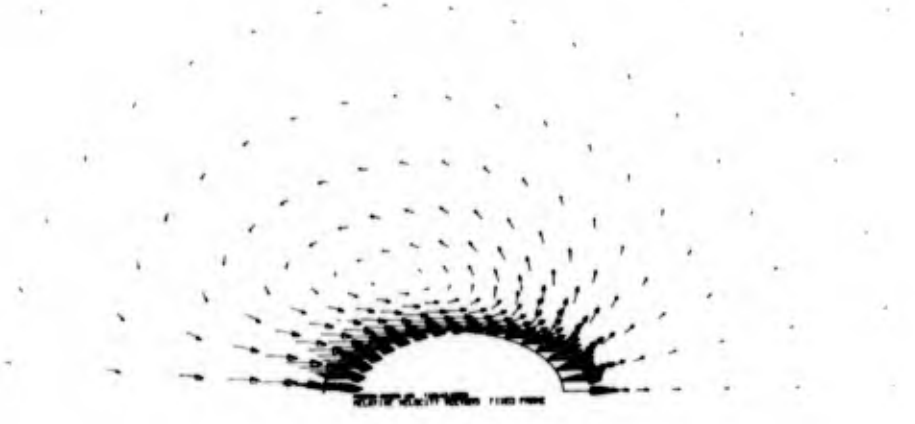

Figure 26. Circulation region of gas particles has moved downstream at time 13.46.

Figure 27. Initial gas particle movement at time .38.

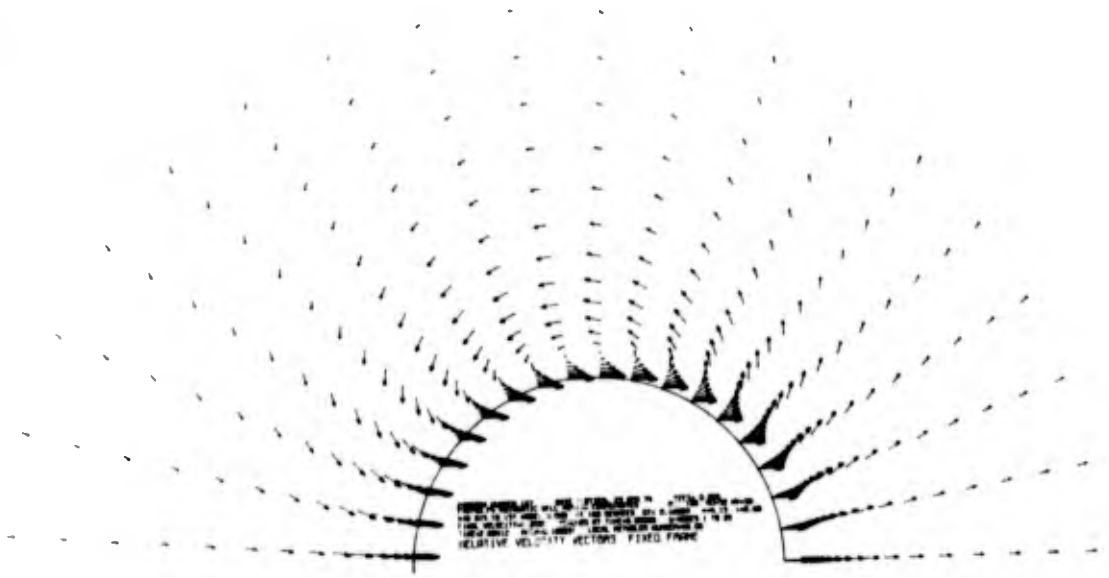

Figure 28. Gas particle movement at time 2.69.

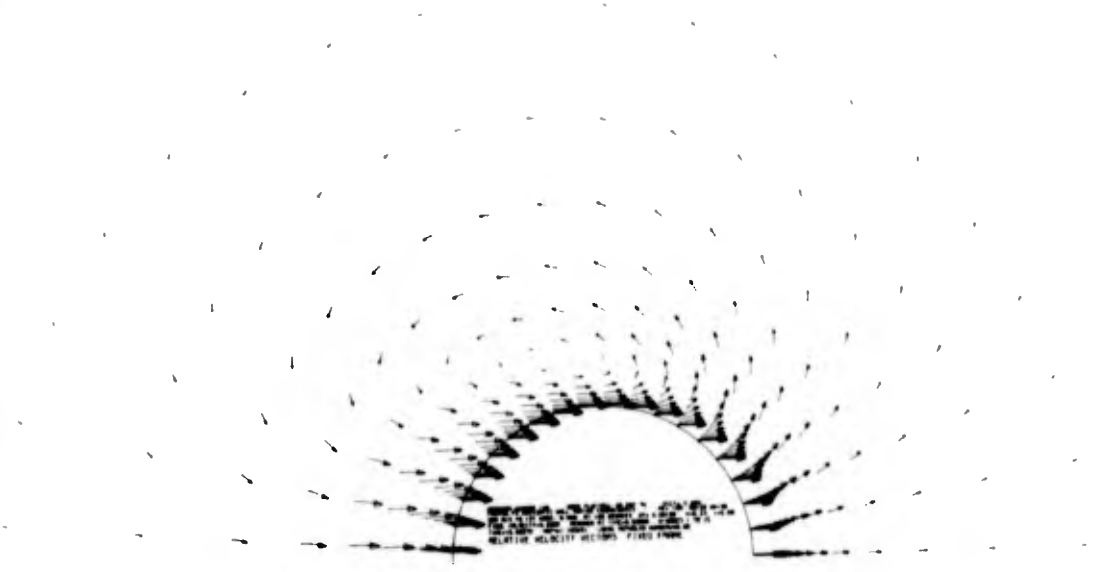

Figure 29. Circulation region of gas particles has moved downstream at time 10.60.

APPENDIX A

Navier-Stokes Equations, Accelerated Reference Frame

The two dimensional Navier-Stokes equations for an ideal compressible viscous gas in an accelerated Cartesian reference frame (x*,y*) are presented here.

The transformation from the fixed frame (x,y) to the accelerated frame (x*,y*) is given by

$$x^* = x - \int_0^t w_x \, dt \quad ,$$

$$y^* = y - \int_0^t w_y \, dt \quad ,$$

where w_x and w_y are the x and y velocities of the accelerated frame relative to the fixed frame.

The primary dependent variables chosen are the density ρ, the x* and y* components of the momentum m_{x^*} and m_{y^*}, and the total energy E. The momentum and total energy are defined as follows:

$$m_{x^*} = \rho V_{x^*} \quad ,$$

$$m_{y^*} = \rho V_{y^*} \quad ,$$

$$E = \rho(e+(V_{x^*}^2 + V_{y^*}^2)/2) \quad ,$$

where V_{x^*} and V_{y^*} are the x* and y* components of the gas velocity, and e is the internal energy. Other dependent variables are the velocity V, temperature T, stress τ, pressure P and heat flux of q.

All dimensional quantities will be nondimensionalized with respect to the following characteristic quantities.

$$L = \text{length} \quad ,$$

$$\frac{c_o}{\sqrt{\gamma}} = \text{velocity} \quad ,$$

$$\frac{L\sqrt{\gamma}}{c_o} = \text{time} \quad ,$$

$$\rho_c = \text{density} \quad .$$

$$\frac{\rho_o c_o^2}{\gamma} = \text{pressure and energy} \quad ,$$

$$\frac{c_o^2}{R\gamma} = \text{temperature} \quad ,$$

where

c_v = specific heat at constant volume ,

c_p = specific heat at constant pressure ,

γ = ratio of specific heats, $\frac{c_p}{c_v}$,

R = gas constant, $c_p - c_v$,

c_o = speed of sound in reference gas .

The scaling yields the following nondimensional quantities.

$$\text{Re} = \text{reference Reynolds number} = \frac{\rho_o c_o L}{\sqrt{\gamma}\,\mu} \quad ,$$

$$\text{Pr} = \text{Prandtl number} = \frac{\mu c_p}{k} \quad ,$$

$$M = \text{Mach number} = \frac{V}{c_o} \quad ,$$

where k is the thermal conductivity and μ is the viscosity.

The Navier-Stokes equations in dimensionless form with the stars dropped for convenience are:

Continuity

$$\frac{\partial \rho}{\partial t} + \frac{\partial m_x}{\partial x} + \frac{\partial m_y}{\partial y} = 0 \quad ,$$

x-momentum

$$\frac{\partial m_x}{\partial t} + \frac{\partial}{\partial x}(m_x V_x) + \frac{\partial}{\partial y}(m_x V_y) = \frac{\partial}{\partial x}[\tau_{xx} - P] + \frac{\partial \tau_{xy}}{\partial y} - \rho \frac{dw_x}{dt} \quad ,$$

y-momentum

$$\frac{\partial m_y}{\partial t} + \frac{\partial}{\partial x}(m_y V_x) + \frac{\partial}{\partial y}(m_y V_y) = \frac{\partial}{\partial y}[\tau_{yy} - P] + \frac{\partial \tau_{xy}}{\partial x} - \rho \frac{dw_y}{dt} \quad ,$$

Total energy

$$\frac{\partial E}{\partial t} + \frac{\partial}{\partial x}(EV_x) + \frac{\partial}{\partial y}(EV_y) = -\frac{\partial q_x}{\partial x} - \frac{\partial q_y}{\partial y}$$

$$+ \frac{\partial}{\partial x}[V_x(\tau_{xx} - P) + V_y \tau_{xy}]$$

$$+ \frac{\partial}{\partial y}[V_x \tau_{yx} + V_y(\tau_{yy} - P)]$$

$$- m_x \frac{dw_x}{dt} - m_y \frac{dw_y}{dt} \quad ,$$

where

$$\tau_{\xi\xi} = \frac{2}{Re}\left[\frac{\partial V_\xi}{\partial \xi} - \left(\frac{\partial V_\xi}{\partial \xi} + \frac{\partial V_\eta}{\partial \eta}\right)/3\right] \quad ,$$

$$\tau_{\xi\eta} = \frac{1}{Re}\left[\frac{\partial V_\xi}{\partial \eta} + \frac{\partial V_\eta}{\partial \xi}\right] \quad ,$$

$$q_\xi = -\frac{\gamma}{(\gamma-1)Pr\,Re}\frac{\partial T}{\partial \xi} \quad ,$$

for $\xi = x,y$ and $\eta = y,x$.

Note that w_x and w_y are relative to the fixed frame.

APPENDIX B

Navier-Stokes Equation in Elliptic Coordinates

This appendix presents the Navier-Stokes equations of Appendix A transformed to elliptic cylindrical coordinates. The transformation from the Cartesian coordinates (x,y) to the elliptic coordinates (u,v) is given by

$$x = c \cosh(u) \cos(v) \quad ,$$

$$y = c \sinh(u) \sin(v) \quad .$$

The notation and variable definitions are identical to those of Appendix A. However, the reference length L of Appendix A is now assumed to be the semi-major axis of the cylinder, $c \cosh(u_o)$, and the momentum is now resolved into u and v components. For convenience, the x and y components of the body velocity w_x and w_y are retained in Cartesian form.

The transformed Navier-Stokes equations [6] are:

Continuity

$$\frac{\partial \rho}{\partial t} + \frac{1}{h^2}\left[\frac{\partial}{\partial u}(h\, m_u) + \frac{\partial}{\partial v}(h\, m_v)\right] = 0 \quad ,$$

u-momentum

$$\frac{\partial m_u}{\partial t} = \frac{1}{h^2}\left\{\frac{\partial}{\partial u}\left[h(\tau_{uu} - m_u V_u - \tau_{vv} + m_v V_v)\right]\right.$$

$$+ 2\frac{\partial}{\partial v}\left[h(\tau_{uv} - m_u V_v)\right] + h\left[\frac{\partial}{\partial u}\left[\tau_{vv} - P - m_v V_v\right]\right.$$

$$\left.\left. - \frac{\partial}{\partial v}\left[\tau_{uv} - m_u V_v\right]\right]\right\} + A\rho\frac{dw_x}{dt} + B\rho\frac{dw_y}{dt} \quad ,$$

v-momentum

$$\frac{\partial m_v}{\partial t} = \frac{1}{h^2}\left\{\frac{\partial}{\partial v}\left[h(\tau_{vv} - m_v V_v - \tau_{uu} + m_u V_u)\right]\right.$$

$$+ 2\frac{\partial}{\partial u}\left[h(\tau_{vu} - m_v V_u)\right] + h\left[\frac{\partial}{\partial v}\left[\tau_{uu} - P - m_u V_u\right]\right.$$

$$\left.\left. - \frac{\partial}{\partial u}\left[\tau_{vu} - m_v V_u\right]\right]\right\} - B\rho\frac{dw_x}{dt} + A\rho\frac{dw_y}{dt} \quad ,$$

Total energy

$$\frac{\partial E}{\partial t} = \frac{1}{h^2}\left\{\frac{\partial}{\partial u}\left[h(V_u(\tau_{uu} - P - E) + V_v \tau_{vu} - q_u)\right]\right.$$

$$+ \frac{\partial}{\partial v}\left[h(V_v(\tau_{vv} - P - E) + V_u \tau_{uv} - q_v)\right]$$

$$\left. + A\left(m_u\frac{dw_x}{dt} + m_v\frac{dw_y}{dt}\right) + B\left(m_u\frac{dw_y}{dt} - m_v\frac{dw_x}{dt}\right)\right\} \quad ,$$

where

$$h = (\sinh^2(u) + \sin^2(v))^{\frac{1}{2}}/\cosh(u_o) \quad ,$$

$$A = \cos(v)\sinh(u)/(h\cosh(u_o)) \quad ,$$

$$B = \sin(v)\cosh(u)/(h\cosh(u_o)) \quad ,$$

$$\tau_{\xi\xi} = \frac{2}{Re}\left\{\frac{1}{h}\frac{\partial V_\xi}{\partial \xi} + \frac{V_\eta}{h^2}\frac{\partial h}{\partial \eta}\right.$$

$$\left. - \frac{1}{3h^2}\left[\frac{\partial}{\partial \xi}(hV_\xi) + \frac{\partial}{\partial \eta}(hV_\eta)\right]\right\} \quad ,$$

$$\tau_{\xi\eta} = \frac{1}{Re}\left\{\frac{\partial}{\partial\xi}\,(V_\eta/h) + \frac{\partial}{\partial\eta}\,(V_\xi/h)\right\} \quad ,$$

$$q_\xi = -\frac{\gamma}{(\gamma-1)\,Pr\,Re\;h}\frac{\partial T}{\partial\xi} \quad ,$$

for $\xi = u,v$ and $\eta = v,u$.

LIST OF REFERENCES

1. Roache, P. J., Computational Fluid Dynamics, pp. 226-228, Hermosa Publishers, Albuquerque, New Mexico, (1972).

2. Liepmann, H. W. and Roshko, A., Elements of Gas Dynamics, p. 91, Eighth Edition, John Wiley & Sons, Inc., (1967).

3. Moretti, G., "Transient and Asymptotically Steady Flow of an Inviscid, Compressible Gas Past a Circular Cylinder", Polytechnic Institute of Brooklyn, PIBAL Report Number 70-20, (1970).

4. MacCormack, R. W., "The Effect of Viscosity in Hypervelocity Impact Cratering", AIAA 7th Aerospace Sciences Meeting, Paper Number 69-354, (1969).

5. Roache, op. cit., pp. 272-275.

6. Woan, C. J. and Akai, T. J., "Basic Gas Dynamic Equations in a Moving Orthogonal Coordinate System", Report T-8, Coordinated Science Laboratory, Urbana, Illinois, (1973).

7. Schlichting, H., Boundary Layer Theory, Sixth Edition, McGraw-Hill Book Co., Inc., New York, (1968).